JACS
JOURNAL OF THE AMERICAN CHEMICAL SOCIETY
pubs.acs.org/JACS
Article

Gas-Phase Synthesis of Coronene through Stepwise Directed Ring Annulation

Shane J. Goettl, Lotefa B. Tuli, Andrew M. Turner, Yahaira Reyes, A. Hasan Howlader, Stanislaw F. Wnuk, Patrick Hemberger,* Alexander M. Mebel,* and Ralf I. Kaiser*

Cite This: J. Am. Chem. Soc. 2023, 145, 15443−15455
Read Online

ABSTRACT: Molecular beam experiments together with electronic structure calculations provide the first evidence of a complex network of elementary gas-phase reactions culminating in the bottom-up preparation of the 24π aromatic coronene ($C_{24}H_{12}$) molecule—a representative peri-fused polycyclic aromatic hydrocarbon (PAH) central to the complex chemistry of combustion systems and circumstellar envelopes of carbon stars. The gas-phase synthesis of coronene proceeds via aryl radical-mediated ring annulations through benzo[*e*]pyrene ($C_{20}H_{12}$) and benzo[*ghi*]perylene ($C_{22}H_{12}$) involving armchair-, zigzag-, and arm-zig-edged aromatic intermediates, highlighting the chemical diversity of molecular mass growth processes to polycyclic aromatic hydrocarbons. The isomer-selective identification of five- to six-ringed aromatics culminating with the detection of coronene is accomplished through photoionization and is based upon photoionization efficiency curves along with photoion mass-selected threshold photoelectron spectra, providing a versatile concept of molecular mass growth processes via aromatic and resonantly stabilized free radical intermediates to two-dimensional carbonaceous nanostructures.

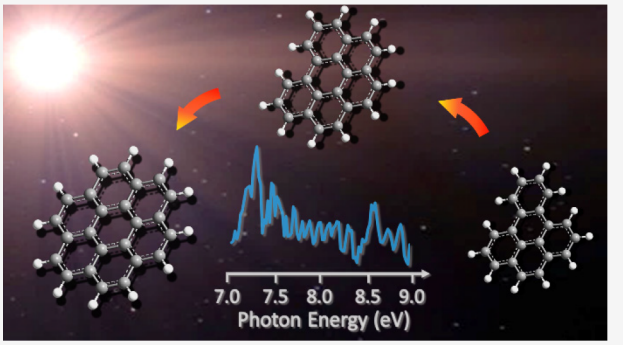

1. INTRODUCTION

Since the very first isolation in 1932 by Scholl and Meyer,[1] coronene ($C_{24}H_{12}$)—a D_{6h} symmetric peri-fused polycyclic aromatic hydrocarbon (PAH) consisting of a central benzene moiety surrounded by six benzene rings—has garnered considerable attention in the realm of two- and three-dimensional carbonaceous nanomaterials. As a planar 24π aromatic system constructed entirely of hexagonal rings, coronene has been implicated in bottom-up synthetic routes[2] to two-dimensional nanostructures such as nanographenes,[3−6] circumarenes,[7] armchair- and zigzag-edge graphene nanoribbons,[2,4,8] and graphene quantum dots (Figure 1).[9] These unique two-dimensional structures hold critical applications in molecular electronics,[10] spintronics,[11] and optoelectronics.[12] While five-membered rings embedded in peri-fused aromatics such as in corannulene ($C_{20}H_{10}$) typically bend the carbon skeleton out-of-plane, molecules like coronene ($C_{24}H_{12}$) with only six-membered rings can still endure curvature[13] when molded into three-dimensional carbonaceous nanostructures like nanowires,[14] chiral[15] and helical[9,16] nanographenes, single-walled[17] and end-capped[18] nanotubes, and fullertubes (C_{90},[19,20] C_{120}[21]) (Figure 1). Such three-dimensional structures have vital applications spanning molecular electronics[22] to medicinal chemistry.[23,24]

Since coronene ($C_{24}H_{12}$) maps onto the basal plane of graphite and graphene nanostructures, complex PAHs are also of fundamental interest to astrochemistry and to the combustion science community as molecular building blocks to carbonaceous nanoparticles referred to as interstellar grains (astrochemistry)[25] and soot particles (combustion),[26] respectively. In deep space, PAHs have been suspected to account for up to 30% of the cosmic carbon budget and are implicated as carriers of diffuse interstellar bands (DIBs)[27] and unidentified infrared (UIR) bands.[28] Sophisticated analyses of carbonaceous chondrites such as Allende[29] and Murchison[30] revealed the presence of PAHs, including coronene ($C_{24}H_{12}$), presumably formed in circumstellar envelopes of carbon-rich asymptotic giant branch (AGB) stars along with planetary nebulae as their descendants.[31] The formation mechanisms in these high-temperature circumstellar environments such as the hydrogen abstraction−acetylene addition (HACA) mechanism[32,33] are assumed to mirror those in hydrocarbon-rich flames, where coronene has been observed in flames of small hydrocarbons (methane, ethylene) and of gasoline surrogates (*n*-heptane, iso-octane, toluene).[34−42] In sooting hydrocarbon

Received: April 12, 2023
Published: July 5, 2023

https://doi.org/10.1021/jacs.3c03816
J. Am. Chem. Soc. 2023, 145, 15443−15455

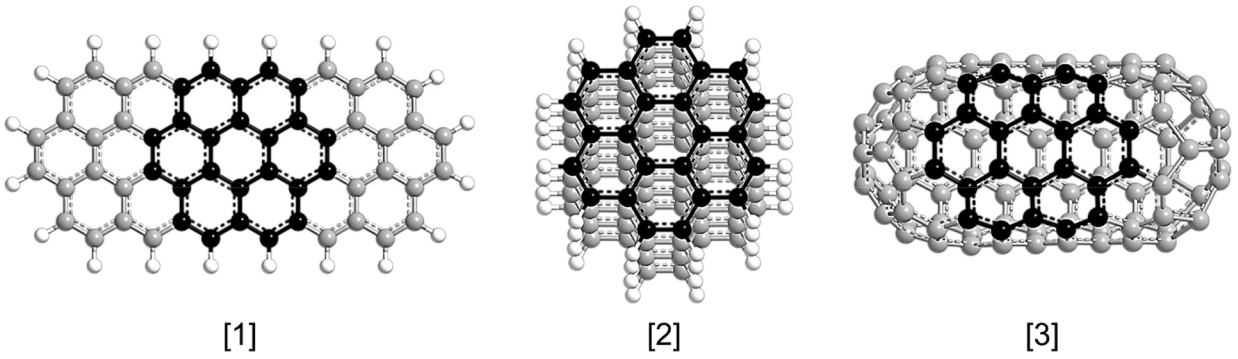

Figure 1. Coronene is emphasized as a molecular building block of 2D and 3D nanostructures such as zigzag nanoribbons (1), nanowires (2), and fullertubes (3). Atoms are color-coded as follows: carbon (gray), carbon in the coronene moiety (black), and hydrogen (white).

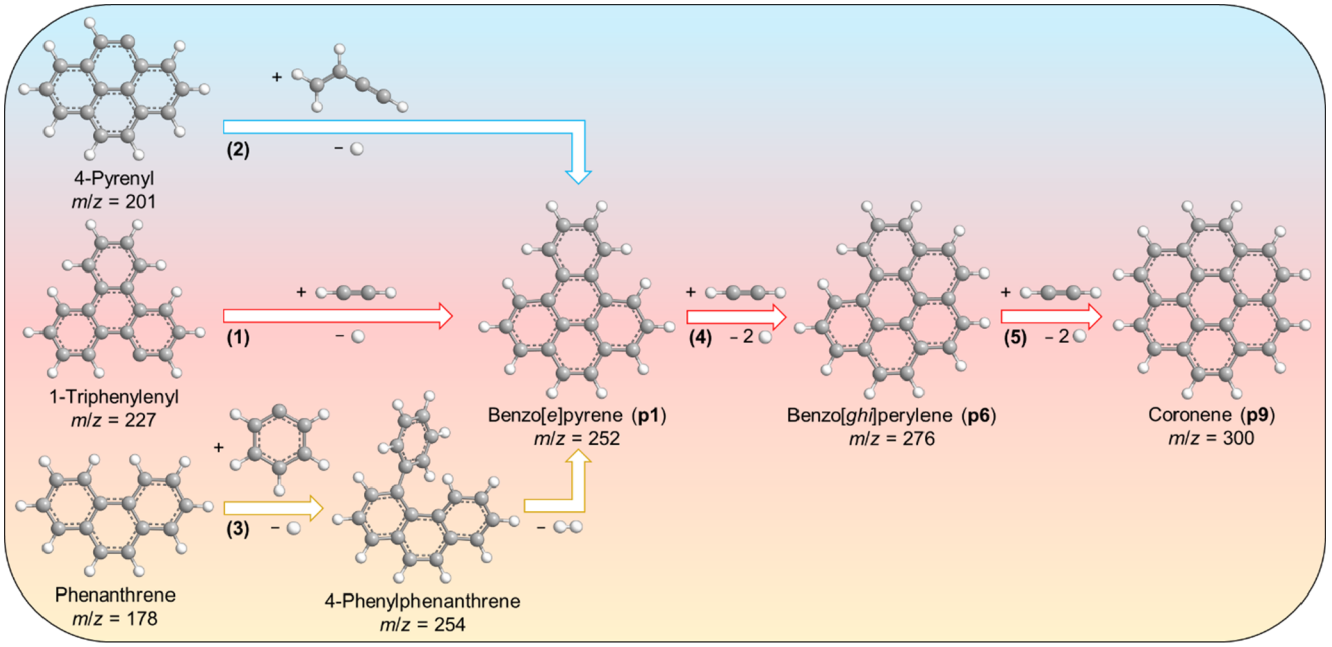

Figure 2. Schematic representation of reaction pathways leading to benzo[*e*]pyrene ($C_{20}H_{12}$, **p1**) from 4-bromopyrene ($C_{16}H_9Br$), 1-bromotriphenylene ($C_{18}H_{11}Br$), and phenanthrene ($C_{14}H_{10}$) via three key molecular mass growth processes: hydrogen abstraction−vinylacetylene addition (HAVA) (blue), hydrogen abstraction−C_2H_2 addition (HACA) (red), and phenyl addition−dehydrocyclization (PAC) (orange), respectively. The schematic continues with the formation of coronene ($C_{24}H_{12}$, **p9**) from benzo[*e*]pyrene through two successive HACA sequences.

flames, coronene ($C_{24}H_{12}$) has been dubbed as a critical precursor in soot nucleation processes—a kinetic bottleneck in the formation of carbonaceous nanostructures.[43−48]

Therefore, an intimate knowledge of the underlying formation mechanisms of coronene in high-temperature terrestrial and circumstellar environments is crucial to our understanding of the molecular mass growth processes to PAHs and carbonaceous nanostructures. High-temperature kinetic flame models are exploited to explore the mechanisms involved in PAH formation not only in combustion processes,[49] but these reaction networks have been also adapted by the astrochemistry community to derive potential pathways to PAHs through circumstellar reaction networks.[50] These models incorporate gas-phase reactions forming PAHs up to coronene ($C_{24}H_{12}$) followed by soot nucleation and aggregation via PAH dimerization.[43] While traditional PAH growth processes have focused on the HACA mechanism,[32,33] more recent models have incorporated resonance-stabilized free radicals (RSFRs) as well as the hydrogen abstraction−vinylacetylene addition (HAVA) and phenyl addition−dehydrocyclization (PAC) pathways.[37−41,47,51−65] However, even these refinements were not able to replicate the observed fractional abundances of coronene ($C_{24}H_{12}$) in, for example, ethylene flames, with modeled coronene abundances falling short by up to an order of magnitude compared to observed data.[52,56] Therefore, the inability to replicate the fractional abundances of coronene ($C_{24}H_{12}$) in combustion flames implies that critical reaction pathways to coronene ($C_{24}H_{12}$) are not properly incorporated in the models. Therefore, an advanced experimental and computational protocol is required to investigate elementary gas-phase reactions yielding coronene ($C_{24}H_{12}$) at elevated temperatures.

Herein, we report on a sophisticated combined molecular beam and computational exploration of the first directed gas-phase synthesis of the 24π aromatic coronene ($C_{24}H_{12}$, **p9**) molecule via benzo[*ghi*]perylene ($C_{22}H_{12}$, **p6**) and benzo[*e*]-pyrene ($C_{20}H_{12}$, **p1**) under high-temperature conditions of up to 1600 K in a chemical microreactor mimicking combustion

https://doi.org/10.1021/jacs.3c03816
J. Am. Chem. Soc. 2023, 145, 15443−15455

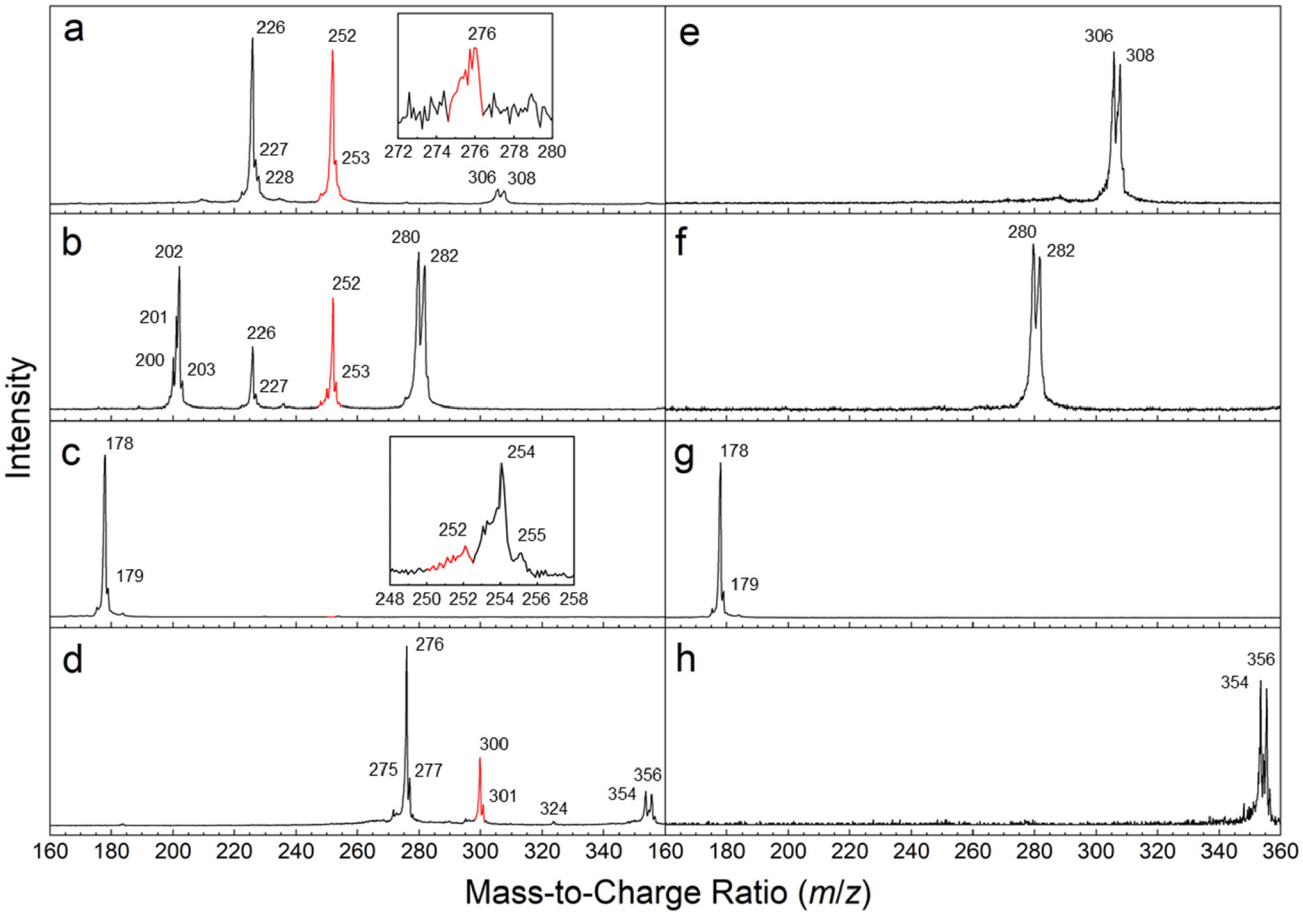

Figure 3. Comparison of photoionization mass spectra taken at a photon energy of 9.00 eV for the (a) acetylene (C_2H_2)−1-bromotriphenylene ($C_{18}H_{11}Br$), (b) vinylacetylene (C_4H_4)−4-bromopyrene ($C_{16}H_5Br$), (c) nitrosobenzene (C_6H_5NO)−phenanthrene ($C_{14}H_{10}$), and (d) acetylene (C_2H_2)−7-bromobenzo[*ghi*]perylene ($C_{22}H_2$) systems at pyrolysis temperatures of 1300 ± 100, 1400 ± 100, 1300 ± 100, and 1500 ± 100 K, respectively; e−h were taken for the same systems with pyrolysis off. The mass peaks of the newly formed $C_{20}H_{12}$ (m/z = 252), $C_{22}H_{12}$ (m/z = 276), and $C_{24}H_{12}$ (m/z = 300) species are highlighted in red.

flames and carbon-rich circumstellar envelopes (Figure 2; Supporting Information). Exploiting an isomer-selective *in situ* product detection coupled with fragment-free photoionization along with photoionization efficiency (PIE) curves and photoion mass-selected threshold photoelectron (ms-TPE) spectra, distinct molecular mass growth mechanisms (HACA, HAVA, PAC) to benzo[*e*] pyrene ($C_{20}H_{12}$, **p1**) were unraveled in the gas phase; these proceed via carbon−carbon bond coupling and ring annulation of 1-triphenylenyl ($C_{18}H_{11}^{\bullet}$), 4-pyrenyl ($C_{16}H_9^{\bullet}$), and phenanthrene ($C_{14}H_{10}$) by acetylene (C_2H_2), vinylacetylene (C_4H_4), and phenyl ($C_6H_5^{\bullet}$), respectively (Figure 2; reactions 1−3) involving aromatic (AR) and RSFRs. We further provide evidence that two successive HACA steps convert benzo[*e*]pyrene ($C_{20}H_{12}$, **p1**) to benzo[*ghi*]perylene ($C_{22}H_{12}$, **p6**) and eventually to coronene ($C_{24}H_{12}$, **p9**) (Figure 2; reactions 4 and 5). The syntheses of bromo precursors for 1-triphenylenyl ($C_{18}H_{11}^{\bullet}$) and 7-benzo[*ghi*]perylenyl ($C_{22}H_{11}^{\bullet}$) radicals are described in the Supporting Information. These findings afford the very first evidence on a facile, isomer-selective high-temperature route to extended aromatic systems from the bottom-up driving molecular mass growth processes of aromatics—coronene ($C_{24}H_{12}$, **p9**)—which act as precursors to soot and interstellar nanoparticles, thus fundamentally changing our conception of the complex carbon chemistry in our galaxy.

2. RESULTS

2.1. Mass Spectra. Five reactions were carried out *in situ* within the chemical microreactor (Table S1). The reactions of 1-triphenylenyl ($C_{18}H_{11}^{\bullet}$) with acetylene (C_2H_2) (**1**), 4-pyrenyl ($C_{16}H_9^{\bullet}$) with vinylacetylene (C_4H_4) (**2**), and phenanthrene ($C_{14}H_{10}$) with phenyl ($C_6H_5^{\bullet}$) (**3**) represent three avenues to explore the gas-phase preparation of benzo[*e*]pyrene ($C_{20}H_{12}$, **p1**) via C18−C2, C16−C4, and C14−C6 carbon−carbon couplings. The elementary reactions of the 1-benzo[*e*]pyrenyl radical ($C_{20}H_{11}^{\bullet}$) with acetylene (C_2H_2) (**4**) and the 7-benzo[*ghi*]perylenyl radical ($C_{22}H_{11}^{\bullet}$) with acetylene (C_2H_2) (**5**) prepare benzo[*ghi*]perylene ($C_{22}H_{12}$, **p6**) and ultimately coronene ($C_{24}H_{12}$, **p9**), respectively.

$$[C_{18}H_{11}]^{\bullet} + C_2H_2 \rightarrow C_{20}H_{12} + H \quad (1)$$

$$[C_{16}H_9]^{\bullet} + C_4H_4 \rightarrow C_{20}H_{12} + H \quad (2)$$

$$C_{14}H_{10} + [C_6H_5]^{\bullet} \rightarrow C_{20}H_{12} + H + H_2 \quad (3)$$

$$[C_{20}H_{11}]^{\bullet} + C_2H_2 \rightarrow C_{22}H_{12} + H \quad (4)$$

$$[C_{22}H_{11}]^{\bullet} + C_2H_2 \rightarrow C_{24}H_{12} + H \quad (5)$$

Representative mass spectra of reactions 1−5 collected at a photon energy of 9.00 eV at reactor temperatures between

https://doi.org/10.1021/jacs.3c03816
J. Am. Chem. Soc. 2023, 145, 15443−15455

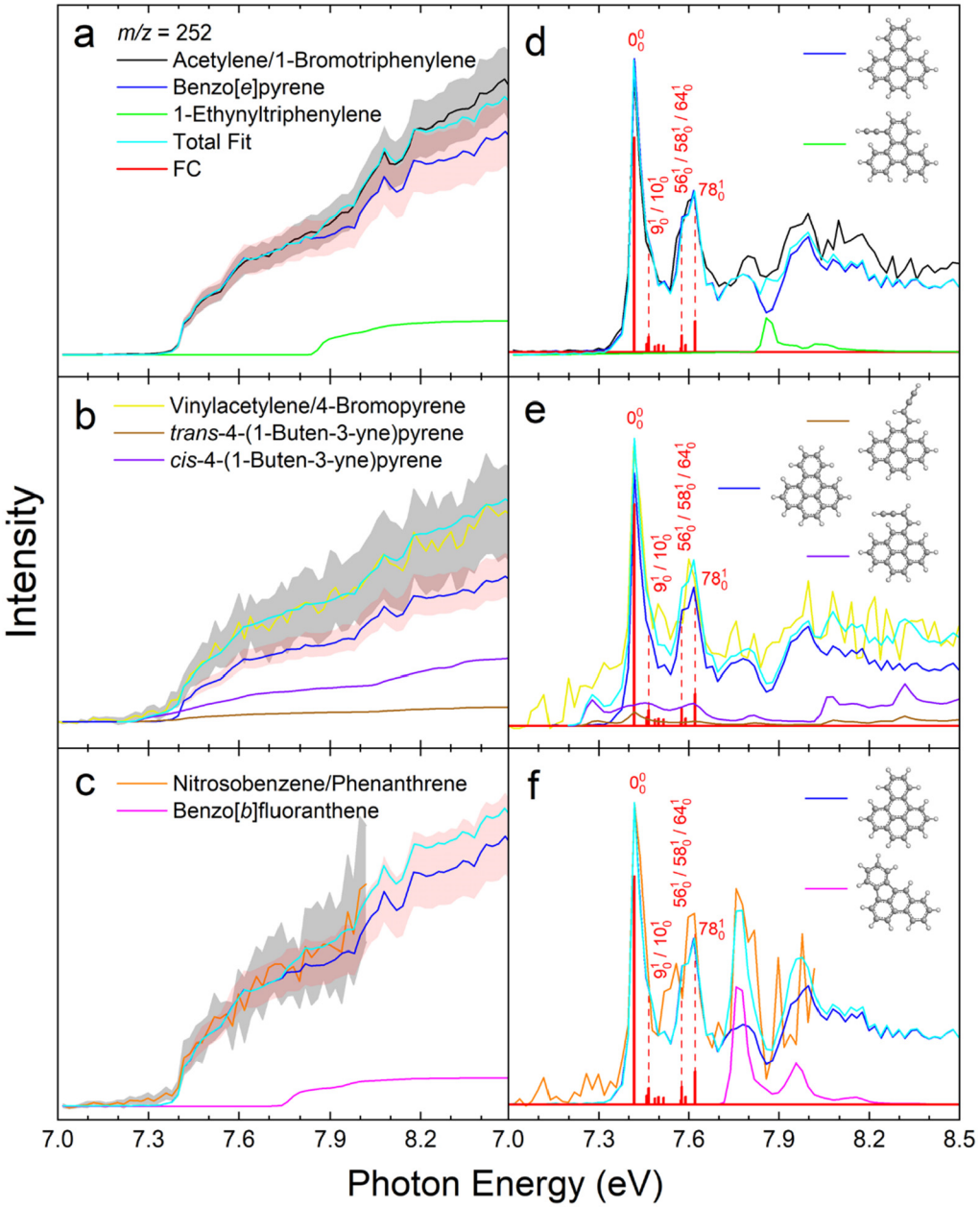

Figure 4. Photoionization efficiency (PIE) curves (a, b, c) and mass-selected threshold photoelectron (ms-TPE) spectra (d, e, and f) relevant to the formation of benzo[*e*]pyrene ($C_{20}H_{12}$) at m/z = 252. Black: acetylene (C_2H_2)−1-bromotriphenylene ($C_{18}H_{11}Br$) experimental curves; blue: benzo[*e*]pyrene reference curves; green: calculated 1-ethynyltriphenylene ($C_{20}H_{12}$) curves; red: calculated Franck−Condon factors (most intense transitions denoted with numbers); yellow: vinylacetylene (C_4H_4)−4-bromopyrene ($C_{16}H_9Br$) experimental curves; brown: calculated *trans*-4-(1-buten-3-yne)pyrene ($C_{20}H_{12}$) curves; violet: calculated *cis*-4-(1-buten-3-yne)pyrene ($C_{20}H_{12}$) curves; orange: nitrosobenzene (C_6H_5NO)−phenanthrene ($C_{14}H_{10}$) experimental curves; magenta: calculated benzo[*b*]fluoranthene ($C_{20}H_{12}$) curves; cyan: total fit for each reaction by summing the individual curves in each frame. The overall error bars (gray- and red-shaded areas) consist of two parts: 1σ error of the PIE curve averaged over the individual scans and ±10% based on the accuracy of the photodiode.

1300 and 1500 K are compiled in Figure 3a−d. A comparison of these data with reference spectra collected at 300 K without pyrolysis (e−h) provides clear evidence of the synthesis of molecules with the molecular formula $C_{20}H_{12}$ (252 amu) as detected via the molecular parent ion at m/z = 252 in the 1-triphenylenyl−acetylene, 4-pyrenyl−vinylacetylene, and phenyl−phenanthrene reactions 1−3 (Figure 3a−c). Subsequent molecular mass growth via HACA leads to a signal at m/z = 276 ($C_{22}H_{12}^+$) (reaction 4) with the benzo[*e*]pyrenyl radical ($C_{20}H_{11}$, 251 amu) formed *in situ* via hydrogen abstraction from $C_{20}H_{12}$ (252 amu) (Figure 3a); this results in a net mass gain of 24 amu. It is important to highlight that the signals at m/z = 252 ($C_{20}H_{12}^+$) and 276 ($C_{22}H_{12}^+$) are absent in the control experiments (Figure 3e−g). Finally, a signal at m/z = 300 ($C_{24}H_{12}^+$) was detected in the 7-benzo[*ghi*]perylenyl−acetylene system (reaction 5), thus showcasing the ultimate formation of $C_{24}H_{12}$ isomer(s). Prominent ion counts are also detectable at mass-to-charge ratios (m/z) of 306 ($C_{18}H_{11}{}^{79}Br^+$) and 308 ($C_{18}H_{11}{}^{81}Br^+$) (reaction 1), 280 ($C_{16}H_9{}^{79}Br^+$) and 282 ($C_{16}H_9{}^{81}Br^+$) (2), 178 ($C_{14}H_{10}^+$) and 179 ($^{13}CC_{13}H_{10}^+$) (3), and 354 ($C_{22}H_{11}{}^{79}Br^+$) and 356 ($C_{22}H_{11}{}^{81}Br^+$) (5). These ions are present in both the *pyrolysis on* and *pyrolysis off* mass

https://doi.org/10.1021/jacs.3c03816
J. Am. Chem. Soc. 2023, 145, 15443−15455

spectra; therefore, they originate from the 1-bromotriphenylene ($C_{18}H_{11}Br$), 4-bromopyrene ($C_{16}H_9Br$), phenanthrene ($C_{14}H_{10}$), and 7-bromobenzo[*ghi*]perylene ($C_{22}H_{11}Br$) reactants, respectively. An additional signal that is only observed with *pyrolysis on* is detailed in the Supporting Information. To summarize, the mass spectra alone afford persuasive evidence of molecular mass growth processes leading to the formation of isomer(s) of $C_{20}H_{12}$ (1−3), $C_{22}H_{12}$ (4), and $C_{24}H_{12}$ (5).

2.2. Photoionization Efficiency Curves and Mass-Selected Threshold Photoelectron Spectra. It is now our objective to ascertain the structural isomer(s) of the $C_{20}H_{12}$, $C_{22}H_{12}$, and $C_{24}H_{12}$ isomers formed from reactions 1−5. To accomplish this goal, PIE curves and ms-TPE spectra are extracted and analyzed. PIE curves depict the ion counts versus the photon energy at a specific mass-to-charge ratio (m/z), whereas ms-TPE spectra select only photoions at the desired m/z in coincidence with the threshold photoelectrons having kinetic energy less than 10 meV. These data are collected between 7.00 and 8.00 eV (3), 7.00 and 8.50 eV (1, 2, 4), and 7.00 and 9.00 eV (5). The experimentally recorded PIE curves and ms-TPE spectra are fit with a linear combination of known calibration curves of distinct structural isomers to identify which isomer(s) is(are) synthesized. Based on the reactant combinations and possible reaction pathways, there are a limited number of $C_{20}H_{12}$, $C_{22}H_{12}$, and $C_{24}H_{12}$ isomers that can be formed as products in each system. This pool is further narrowed by analyzing the ionization potentials and PIE/ms-TPE spectra of each isomer, and only those that match the experimental data are verified to form. The exploitation of PIE curves and ms-TPE spectra in tandem enables isomer-selective identification of hydrocarbon molecules (Supporting Information, Figures S7 and S8).[66−74]

Reaction 1. First, data were extracted at m/z = 252 ($C_{20}H_{12}^+$) for reactions 1−3 (Figure 4). The experimental PIE curve exhibits an ionization onset of 7.40 ± 0.05 eV, which is matched very well by the benzo[*e*]pyrene (**p1**) reference curve depicting an onset of 7.40 ± 0.05 eV (Figure 4a). However, above 7.8 eV, the benzo[*e*]pyrene (**p1**) spectrum cannot entirely account for the experimental signal intensity; therefore, a calculated PIE for 1-ethynyltriphenylene (**p2**) was incorporated to fit the data at these higher photon energies. The linear combination of benzo[*e*]pyrene (**p1**) and 1-ethynyltriphenylene (**p2**) offers a good match for the experimental curve, with ion counts at 8.50 eV at fractions of 84 ± 8% and 16 ± 3%, respectively. It is important to note that the actual branching ratios of benzo[*e*]pyrene (**p1**) versus 1-ethynyltriphenylene (**p2**) require the knowledge of their absolute photoionization cross sections, which are unknown; further, they cannot be provided computationally with sufficient accuracy.[75] Next, the PIE findings are compared with those of ms-TPES (Figure 4d). The experimental spectrum reveals a sharp fundamental (0_0^0) transition at 7.40 ± 0.05 eV followed by a broader peak centered at 7.60 ± 0.05 eV, a small peak at 7.80 ± 0.05 eV, and yet another broad peak centered at 8.00 ± 0.05 eV. The benzo[*e*]pyrene (**p1**) reference spectrum matches these positions quite well; the only deficiency lies at 7.85−7.90 eV, which shows a strong dip compared to the experimental spectrum. However, this is remedied by incorporating the calculated 1-ethynyltriphenylene (**p2**) spectrum, which exhibits several transitions in this energy range. Overall, the reaction 1 PIE findings are mirrored in the ms-TPES data featuring an excellent overlap between the experimental spectrum and the fit of two contributions: major benzo[*e*]pyrene (**p1**) and minor 1-ethynyltriphenylene (**p2**).

Reaction 2. The PIE for reaction 2 reveals an ionization onset of 7.20 ± 0.05 eV (Figure 4b), which may indicate that other isomers, aside from benzo[*e*]pyrene (**p1**), are present in the molecular beam as well. This low-energy section of the PIE can be fit using calculated PIE curves of *cis*- and *trans*-4-(1-buten-3-yne)pyrene (**p4** and **p3**); however, a signal above 7.40 eV cannot be accounted for by these two isomers alone. An incorporation of the benzo[*e*]pyrene (**p1**) reference curve fits well with the experimental PIE at photon energies above 7.40 eV. Essentially, a linear combination of benzo[*e*]pyrene (**p1**) with the *cis*- and *trans*-4-(1-buten-3-yne)pyrene (**p4** and **p3**) isomers with relative ion counts at 8.50 eV of 65 ± 4%, 29 ± 3%, and 6 ± 5%, respectively, produces an excellent match to the experimental curve. The ms-TPES features a reduced signal-to-noise ratio compared with that observed for reaction 1; nevertheless, the ms-TPES exhibits identical peaks at 7.40 ± 0.05, 7.60 ± 0.05, 7.80 ± 0.05, and 8.00 ± 0.05 eV in addition to a small broad feature at 7.30 ± 0.05 eV (Figure 4e). Using *cis*- and *trans*-4-(1-buten-3-yne)pyrene (**p4** and **p3**) to fit the minor peak at 7.30 eV *and* benzo[*e*]pyrene (**p1**) to replicate the data above 7.40 eV provides a reasonably good match to the experimental spectrum.

Reaction 3. The experimental PIE for reaction 3 displays an ionization onset of 7.35 ± 0.05 eV, which lies within the error of the benzo[*e*]pyrene (**p1**) reference onset of 7.40 ± 0.05 eV (Figure 4c). The full experimental PIE curve can be fit by exploiting only the benzo[*e*]pyrene (**p1**) PIE; however, this is not the case for the ms-TPES (Figure 4f). Here, a large peak spanning from 7.75 ± 0.05 to 7.85 ± 0.05 eV cannot be accounted for by the benzo[*e*]pyrene (**p1**) reference spectrum; therefore, the calculated ms-TPES of benzo[*b*]fluoranthene (**p5**), which features a strong peak between 7.75 ± 0.05 and 7.85 ± 0.05 eV, was added. A linear combination of the benzo[*e*]pyrene (**p1**) *and* benzo[*b*]fluoranthene (**p5**) ms-TPE spectra offers a reasonable fit of the experimental spectrum. Incorporating both isomers in the fit for the experimental PIE also provides a good match, too, with ion counts for benzo[*e*]pyrene (**p1**) and benzo[*b*]fluoranthene (**p5**) at 8.00 eV of 87 ± 2% and 13 ± 4%, respectively. The result that the experimental PIE can be fit with both isomers or with only benzo[*e*]pyrene (**p1**), while the ms-TPES can only be fit with both isomers, highlights the merits of the PEPICO technique for sensitive isomer-specific determination of complex molecules. Additionally, Franck−Condon factors (FC) were calculated for the benzo[*e*]pyrene (**p1**) vibronic transitions from the neutral ground electronic state to the cation ground electronic state, which are shown as red vertical lines in Figure 4d−f. The origin band at 7.42 ± 0.05 eV matches the most intense peak for all three reactions, while the next three most intense lines at 7.46 ± 0.05, 7.58 ± 0.05, and 7.62 ± 0.05 eV can be assigned to the $9_0^1/10_0^1$, $56_0^1/58_0^1/64_0^1$, and 78_0^1 transitions, respectively, which coincide with distinct peaks or shoulders of the experimental spectra (Figure 4d−f) and represent the vibrational fingerprint benzo[*e*]pyrene. All together, we have provided evidence for the formation of benzo[*e*]pyrene ($C_{20}H_{12}$, **p1**) from reactions 1−3.

Reaction 4. The data were analyzed for m/z = 276 ($C_{22}H_{12}^+$) for reaction 4 (Figure 5). The experimental PIE curve can be fit solely with a benzo[*ghi*]perylene (**p6**) reference PIE, both of which have an ionization onset of 7.15 ± 0.05 eV. Signal intensity was very weak at m/z = 276,

https://doi.org/10.1021/jacs.3c03816
J. Am. Chem. Soc. 2023, 145, 15443−15455

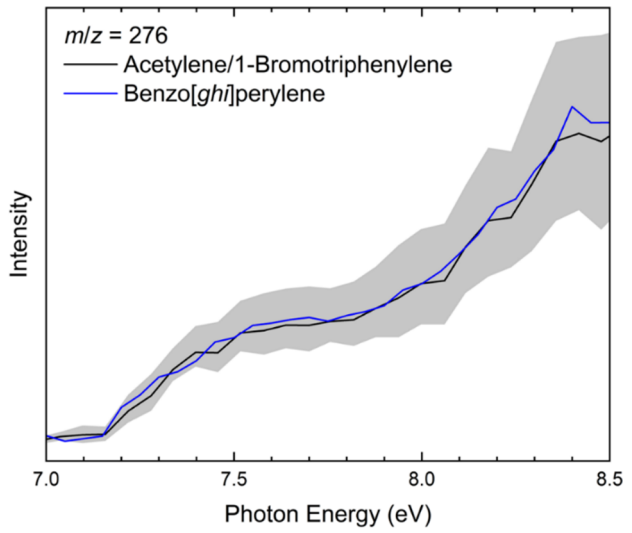

Figure 5. Photoionization efficiency (PIE) curves at m/z = 276 ($C_{22}H_{12}$). Black: experimentally derived PIE curve; blue: benzo[*ghi*]-perylene reference PIE curve. The overall error bars (gray area) consist of two parts: 1σ error of the PIE curve averaged over the individual scans and ±10% based on the accuracy of the photodiode.

and thus we were unable to obtain a reliable ms-TPES; however, the excellent overlap between the experimental and reference PIEs alone provides evidence on the formation of benzo[*ghi*]perylene (**p6**) from reaction 4.

Reaction 5. Finally, data were extracted at m/z = 300 ($C_{24}H_{12}^{+}$) for reaction 5 (Figure 6). Inspecting first the PIE curve, only a single isomer—coronene (**p9**)—is necessary to provide a reasonable fit of the experimental data (Figure 6a). The experimental ionization onset occurs at 7.30 ± 0.05 eV, which shows an excellent agreement within error to the coronene (**p9**) reference onset at 7.310 ± 0.005 eV from Bréchignac et al.[68] The ms-TPE spectrum features a strong peak at 7.30 ± 0.05 eV, which is matched by the coronene (**p9**) reference spectrum (Figure 6b) and corresponds to the origin band transition (0_0^0). The reference also displays a peak at 7.36 eV, which is reflected in the experimental spectrum as a shoulder and can be attributed to the in-plane ring deformation (18_0^1), followed by three peaks in close proximity, all within 7.40 to 7.60 eV, aligning well with the experimental peaks. The first lies at 7.44 eV and is likely due to the overtone 18_0^2; however, the second and third peaks at 7.48 and 7.54 eV are more difficult to assign. There are multiple transitions very near each other around 7.48 eV,[68] with the most intense being the C−C stretching mode 4_0^1, and since our scan step size was 0.02 eV, each transition in this region cannot be individually resolved; thus the peak at 7.48 eV potentially arises from the 10_0^1, 9_0^1, and/or 4_0^1 transitions. Likewise, the peak at 7.54 eV can be tentatively assigned to the combination band ($18_0^1 4_0^1$) of the two most intense individual transitions. The next definitive peak in the experimental ms-TPES lies around 8.60 ± 0.05 eV, also matching the coronene (**p9**) reference. This peak belongs to the origin bands of the coronene cation electronic excited states 1^2B_{2g} and 1^2B_{3g}.[76] It is important to note that ion counts from 7.10 to 7.25 likely originate from hot and sequence bands, which results in a spectrum containing spectral broadening from low collisional cooling and larger scan steps as compared to the reference spectrum.[77] Overall, both the PIE curves and ms-TPE spectra evidence the formation of coronene ($C_{24}H_{12}$, **p9**) from the reaction of acetylene (C_2H_2) with a 7-benzo[*ghi*]perylenyl radical ($C_{22}H_{11}^{\bullet}$).

3. DISCUSSION

In the case of complex reactions involving polyatomic reactants, it is essential to combine the experimental results

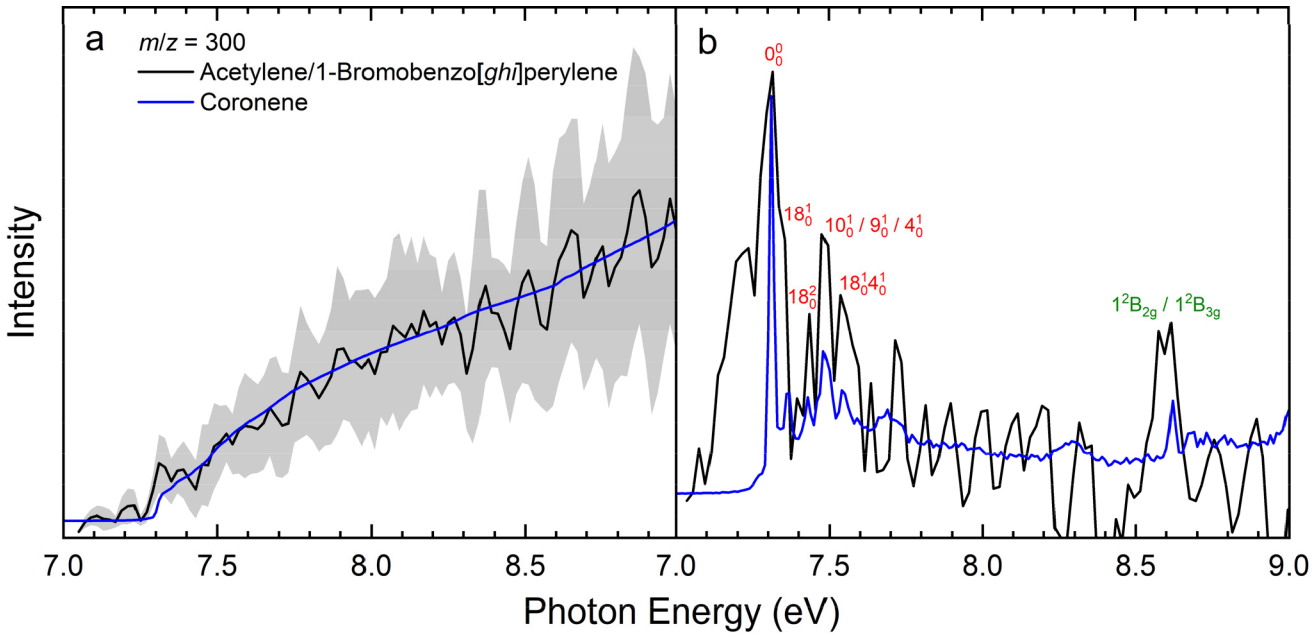

Figure 6. Photoionization efficiency (PIE) curves (a) and mass-selected threshold photoelectron (ms-TPE) spectra (b) relevant to the formation of coronene ($C_{24}H_{12}$) at m/z = 300. Black: acetylene (C_2H_2)−7-bromobenzo[*ghi*]perylene ($C_{22}H_{11}Br$) experimental curves; blue: coronene reference curves from Bréchignac et al;[68] red: vibronic transitions from the coronene neutral electronic ground state to the cation electronic ground state; green: vibronic transition from the coronene neutral electronic ground state to the cation first electronic excited state. The overall error bars (gray-shaded areas) consist of two parts: 1σ error of the PIE curve averaged over the individual scans and ±10% based on the accuracy of the photodiode.

https://doi.org/10.1021/jacs.3c03816
J. Am. Chem. Soc. 2023, 145, 15443−15455

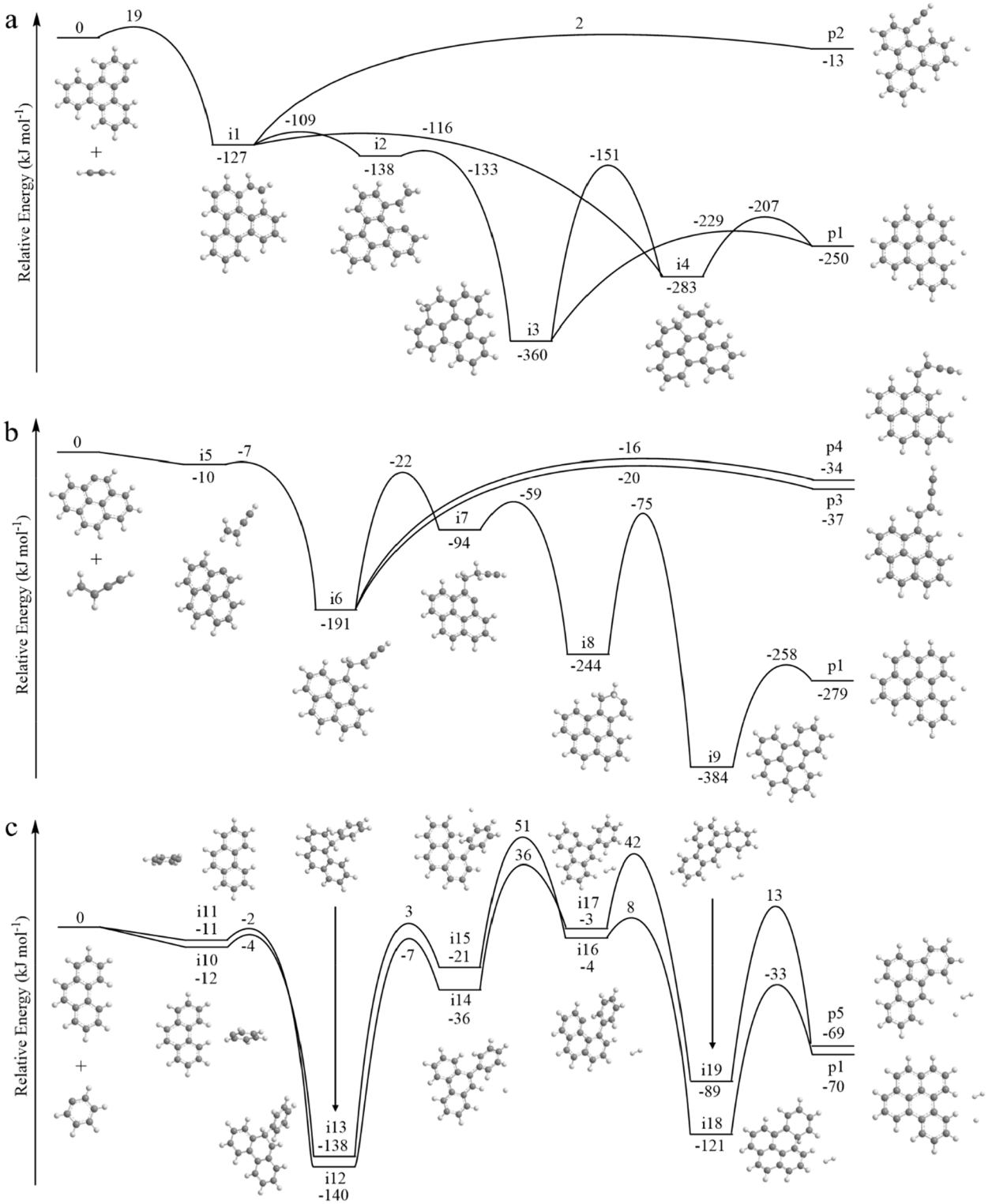

Figure 7. Potential energy diagrams leading to $C_{20}H_{12}$ isomers from the acetylene (C_2H_2)−1-triphenylenyl ($C_{18}H_{11}^{\bullet}$) (a), vinylacetylene (C_4H_4)−4-pyrenyl ($C_{16}H_9^{\bullet}$) (b), and phenyl ($C_6H_5^{\bullet}$)−phenanthrene ($C_{14}H_{10}$) (c) reactions calculated at the G3(MP2,CC)//B3LYP/6-311G(d,p) level.

with electronic structure calculations of potential energy surfaces (PES) leading to benzo[*e*]pyrene (**p1**), benzo[*ghi*]-perylene (**p6**), and coronene (**p9**) via reactions 1−5. *First*, the PESs for reactions 1−3 preparing the gas-phase benzo[*e*]-pyrene are depicted in Figure 7. Reaction 1 (Figure 7a) is initiated by the addition of acetylene (C_2H_2) with one of the carbon atoms to the radical center of the 1-triphenylenyl ($C_{18}H_{11}^{\bullet}$) radical, forming intermediate **i1** via an entrance barrier of 19 kJ mol^{-1}. Intermediate **i1** can simply lose a hydrogen atom to form the side chain $C_{20}H_{12}$ product isomer 1-ethynyltriphenylene (**p2**) through a transition state (TS) positioned 2 kJ mol^{-1} above the initial reactants; conversely, **i1** may undergo a series of isomerization steps involving, for example, ring closure, eventually leading to benzo[*e*]pyrene

https://doi.org/10.1021/jacs.3c03816
J. Am. Chem. Soc. 2023, 145, 15443−15455

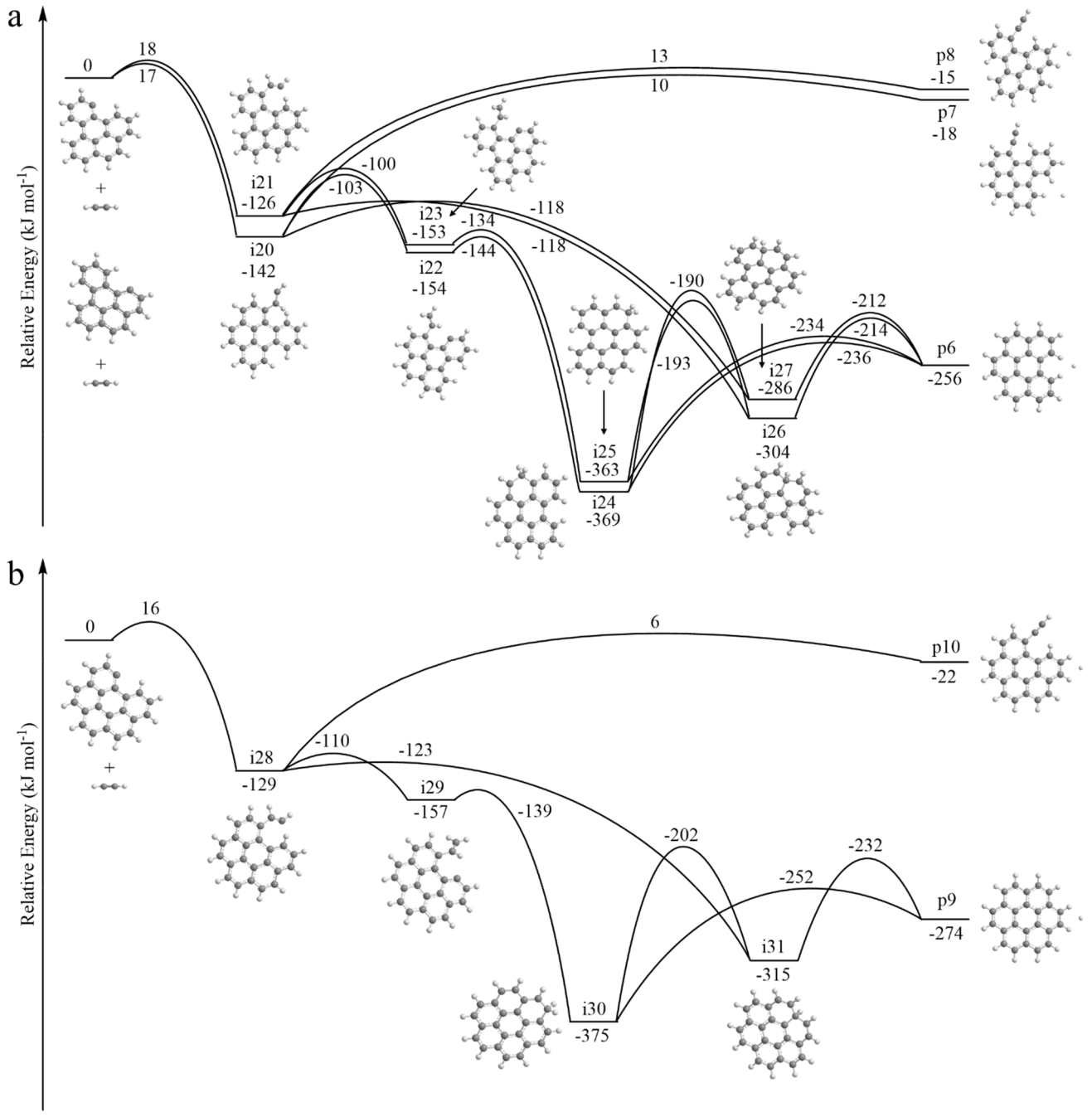

Figure 8. Potential energy diagrams leading to $C_{22}H_{12}$ isomers from the acetylene (C_2H_2)−1-benzo[*e*]pyrenyl ($C_{20}H_{11}^{\bullet}$) reaction (a) and $C_{24}H_{12}$ isomers from the acetylene (C_2H_2)−7-benzo[*ghi*]perylenyl ($C_{22}H_{11}^{\bullet}$) reaction (b) calculated at the G3(MP2,CC)//B3LYP/6-311G(d,p) level.

(**p1**). This process involves a hydrogen atom migration from the C12 carbon of **i1** to the terminal carbon of the side chain (**i1** → **i2**), a six-membered ring closure via a barrier of only 5 kJ mol^{-1} (**i2** → **i3**), and an atomic hydrogen loss from the CH_2 group accompanied by aromatization to benzo[*e*]pyrene (**i3** → **p1**). Additional pathways include an immediate six-membered-ring closure from **i1** to **i4** and subsequent hydrogen atom loss to **p1**, as well as hydrogen atom migration connecting **i3** and **i4**. Overall, the acetylene (C_2H_2)−1-triphenylenyl ($C_{18}H_{11}^{\bullet}$) reaction results in the formation of benzo[*e*]pyrene (**p1**) in an exoergic reaction featuring an entrance barrier via HACA, limiting this process to high-temperature environments such as combustion flames and circumstellar envelopes.

Reaction 2 (Figure 7b) forms an initial van der Waals reactant complex, effectively submerging the subsequent barrier to addition by 7 kJ mol^{-1} below the separated reactants. The following process entails the addition of the 4-pyrenyl ($C_{16}H_9^{\bullet}$) radical center to the terminal carbon of the vinyl moiety of vinylacetylene (C_4H_4), forming doublet radical intermediate **i6**. From here, **i6** may undergo unimolecular decomposition through atomic hydrogen loss, forming the side chain product isomers *cis*- and *trans*-4-(1-buten-3-yne)pyrene (**p4** and **p3**), or follows a complex set of isomerization reactions. These include hydrogen migration from the *ortho* position of the attacked ring to the β carbon of the vinylacetylene moiety (**i6** → **i7**), a facile six-membered ring closure (**i7** → **i8**), an additional hydrogen migration from the

https://doi.org/10.1021/jacs.3c03816
J. Am. Chem. Soc. 2023, 145, 15443−15455

C10 to C11 carbon of **i8** (**i8** → **i9**), and finally atomic hydrogen loss with aromatization to benzo[*e*]pyrene (**i9** → **p1**). The vinylacetylene (C_4H_4)−4-pyrenyl ($C_{16}H_9^{\bullet}$) reaction is a typical reaction of the HAVA mechanism and a *de facto* barrierless reaction featuring a submerged entrance channel with all intermediates, products, and transition states lying below the energy of the separate reactants; therefore, the formation of benzo[*e*]pyrene (**p1**) through reaction 2 can occur in low-temperature environments such as cold molecular clouds.

For reaction 3, the phenyl radical ($C_6H_5^{\bullet}$) can add to any of the C1−C10 carbons of phenanthrene ($C_{14}H_{10}$); however, only addition to the carbons at a terminal edge of a carbon bay, i.e., symmetric C4 and C5, will yield benzo[*e*]pyrene (**p1**) identified in the experiments. In detail (Figure 7c), two reaction pathways are critical: the first with the phenyl radical approaching the four-carbon bay and the second with the phenyl radical approaching a three-carbon bay. Unlike typical PAC mechanisms investigated thus far for smaller PAHs,[78] both cases proceed first to a van der Waals complex upon initial interaction of the reactants due to enhanced long-range interactions in the entrance channels effectively submerging the entrance barrier 4 and 2 kJ mol^{-1} below the reactants' energy level, respectively. For the former, the phenyl radical adds to the C4 carbon of phenanthrene, forming **i13** followed by stabilization via hydrogen atom loss to **i15**. Secondary reactions of hydrogen atoms with **i15** lead, through hydrogen abstraction, to **i16** followed by six-membered-ring cyclization to **i18** and finally hydrogen atom loss accompanied by aromatization to benzo[*e*]pyrene (**p1**). Turning to the second reaction pathway, the phenyl radical adds to the C9 carbon of phenanthrene, forming **i12**. From here, the reaction follows the same mechanistic steps from **i12** → **i14** → **i17** as those shown for **i13** → **i15** → **i16**. From **i17**, the intermediate undergoes facile five-membered ring closure to **i19** and then atomic hydrogen loss coupled with aromatization to benzo[*b*]-fluoranthene (**p5**). While the reactions are overall exoergic and the entrance barriers are submerged below the energy of the reactants for both pathways, there are still substantial barriers that lie higher in energy than the reactants, thus restraining reaction 3 to high-temperature environments. Altogether, the computations for reactions 1−3 demonstrate the facile formation of benzo[e]pyrene (**p1**) via three distinct reaction mechanisms—HACA, HAVA, and PAC—which correlate well with the aforementioned experimental findings.

The potential energy diagrams for reactions 4 and 5 eventually preparing coronene (**p9**) are compiled in Figure 8. For reaction 4, the benzo[*e*]pyrenyl ($C_{20}H_{11}^{\bullet}$) reactant was generated *in situ* by hydrogen abstraction from the benzo[*e*]-pyrene (**p1**) product of reaction 1. Therefore, the benzo[*e*]-pyrenyl radical center could be located at any of the outer carbon atoms. However, the reaction can only lead to the target molecule benzo[*ghi*]perylene (**p6**) if the radical center is on the C1 or C12 carbon of benzo[*e*]pyrenyl, and thus, only these two pathways are considered here (Figure 8a). Both pathways are similar to that of reaction 1, albeit with distinct energies of stabilization of the intermediates, transition states, and products; the initial acetylene addition proceeds with an entrance barrier followed by hydrogen migration and ring closure, leading eventually to benzo[*ghi*]perylene (**p6**) via hydrogen atom loss. Likewise, the final reaction in the sequence to coronene (**p1**), reaction 5, mirrors the aforementioned pathway starting with the 7-benzo[*ghi*]-perylenyl radical ($C_{22}H_{11}^{\bullet}$) addition to acetylene via a barrier of 16 kJ mol^{-1} followed by hydrogen migration and ring cyclization prior to unimolecular decomposition via hydrogen atom loss to coronene (**p9**) in an overall exoergic reaction (−274 kJ mol^{-1}).

4. CONCLUSION

Our combined molecular beam and computational study evidences the first bottom-up synthesis of the 24π aromatic coronene ($C_{24}H_{12}$, **p9**) molecule—the simplest representative of a peri-fused polycyclic aromatic hydrocarbon carrying a central benzene moiety surrounded by six benzene rings. The complex chain of elementary gas-phase reactions is initiated by three aryl-radical-mediated ring annulation mechanisms, i.e., HACA (1), HAVA (2), and PAC (3), involving armchair, zigzag, and arm-zig edged aromatics, respectively, highlighting the chemical diversity of PAH growth pathways leading via benzo[*e*]pyrene ($C_{20}H_{12}$, **p1**) and benzo[*ghi*]perylene ($C_{22}H_{12}$, **p6**) intermediates to coronene ($C_{24}H_{12}$, **p9**). The isomer-selective identification of five- to six-ringed aromatics culminating with the detection of coronene ($C_{24}H_{12}$, **p9**) in this multifaceted molecular mass growth process is achieved through fragment-free vacuum ultraviolet photoionization along with PIE curves and photoion ms-TPE spectra. The high-temperature reaction conditions of up to 1500 K explored here efficiently replicate the conditions in high-temperature combustion systems and circumstellar envelopes of carbon stars along with planetary nebulae as their descendants. The convergence of molecular beam and computational studies discloses an advancement to such a level that polyatomic reactions involving aromatic radical transients relevant to extreme astrochemical and combustion chemistry conditions can be unraveled in concert, thus offering a versatile strategy to explore the exotic chemistry of complex polycyclic aromatic hydrocarbons via resonantly stabilized *and* aromatic free radicals in deep space. These processes may ultimately be expanded to two- and three-dimensional carbonaceous nanostructures, such as graphenes and nanobowls, as molecular building blocks of soot and interstellar grains, thereby advancing our knowledge of the chemistry of carbonaceous matter in the universe.

5. MATERIALS AND METHODS

5.1. Experimental Methods. The experiments were conducted at the X04DB beamline of the Swiss Light Source at the Paul Scherrer Institute utilizing a resistively heated silicon−carbide (SiC) chemical microreactor coupled to a molecular beam apparatus operated with a double velocity map imaging (VMI) photoelectron photoion coincidence spectrometer.[79−84] Four reaction systems were studied: acetylene (C_2H_2) with 1-bromotriphenylene ($C_{18}H_{11}Br$), vinylacetylene (C_4H_4) with 4-bromopyrene ($C_{16}H_9Br$), nitrosobenzene (C_6H_5NO) with phenanthrene ($C_{14}H_{10}$), and acetylene (C_2H_2) with 7-bromobenzo[*ghi*]perylene ($C_{22}H_{11}Br$). Briefly, 1-bromotriphenylene ($C_{18}H_{11}Br$), 4-bromopyrene ($C_{16}H_9Br$), phenanthrene ($C_{14}H_{10}$; 98%; Sigma-Aldrich), and 7-bromobenzo[*ghi*]perylene ($C_{22}H_{11}Br$) were heated at 423 ± 1, 403 ± 1, 358 ± 1, and 513 ± 1 K in a high-vacuum oven located in the source chamber and were seeded in acetylene (C_2H_2; ≥99.5%; PANGAS; acetone traces removed via ethanol/dry ice bath), vinylacetylene (C_4H_4; 5% in helium, Applied Gas Inc.), nitrosobenzene (C_6H_5NO; 97%, Sigma-Aldrich; seeded at <1% in helium), and acetylene at backing pressures of 100, 100, 125, and 220 mbar, respectively. The gas mixtures were introduced through a 0.2 mm nozzle to the SiC microreactor, which had a 1 mm inner diameter and heated length of 20 mm kept at 1300 ± 100, 1400 ± 100, 1300 ± 100, and 1500 ± 100 K, respectively. Products formed

https://doi.org/10.1021/jacs.3c03816
J. Am. Chem. Soc. 2023, 145, 15443−15455

attained supersonic expansion upon exiting the reactor and passed through a 2 mm diameter skimmer into the spectrometer chamber, where they were photoionized by vacuum ultraviolet (VUV) light at photon energies from 7 to 9 eV. Photoions and photoelectrons are extracted by a constant electric field of 218 V cm^{-1} and collected in coincidence via VMI on two position-sensitive delay-line anode detectors (Roentdek DLD40). These experiments provide PIE curves, which depict ion counts versus photon energy at a specific mass-to-charge ratio and ms-TPE spectra, which are collected from the same method as the PIE curves while selecting only photoions at the desired m/z in coincidence with the photoelectrons having a kinetic energy less than 10 meV. The hot electron signal was subtracted from the threshold (kinetic energy less than 10 meV) electrons using the procedure by Sztaray et al.[85] The PIE curves and ms-TPE spectra were corrected due to the Stark shift[86] and normalized to the photon flux. Reference curves for benzo[e]pyrene were taken by subliming the sample in a high-vacuum oven at 423 ± 1 K, seeding it in helium at a backing pressure of 115 mbar, and passing it through the SiC reactor without heating into the spectrometer chamber.

5.2. Computational Methods. Geometries of the reactants, products, intermediates, and transition states for reactions 1−5 were optimized using the density functional theory (DFT) B3LYP method[87,88] with the 6-311G(d,p) basis set, and vibrational frequencies of all species were computed at the same B3LYP/6-311G(d,p) level of theory. Single-point energies at the optimized geometries were refined employing coupled cluster CCSD(T) and second-order Møller−Plesset perturbation theory MP2 calculations, with the final G3(MP2,CC) energy computed as[89−91]

$$E[\mathrm{G3(MP2,\ CC)}] = E[\mathrm{CCSD(T)/6\text{-}31G(d)}] + E[\mathrm{MP2/G3Large}] - E[\mathrm{MP2/6\text{-}31G(d)}] + \mathrm{ZPE[B3LYP/6\text{-}311G(d,\ p)}]$$

The model chemistry G3(MP2,CC) scheme provides a chemical accuracy of 0.01−0.02 Å for bond lengths, 1−2° for bond angles, and 3−6 kJ mol^{-1} for relative energies of hydrocarbons, their radicals, reaction energies, and barrier heights in terms of average absolute deviations.[91]

Adiabatic ionization energies of various $C_{20}H_{12}$, $C_{22}H_{12}$, and $C_{24}H_{12}$ products were also computed using the G3(MP2,CC)//B3LYP/6-311G(d,p) method with zero point energy (ZPE) corrections; the expected accuracy in this case is ±0.05 eV. Moreover, ionization Franck−Condon factors at 0 K needed for a comparison with the experimental ms-TPE spectra were calculated using B3LYP/6-311G(d,p)-optimized geometries and corresponding vibrational frequencies of the neutral and cationic species using the methodology implemented by Barone and co-workers.[92] Electronic excitation energies of the *trans*-4-(1-buten-3-yne)pyrene cation were estimated within the time-dependent (TD)-DFT method[93,94] with the ωB97XD functional[95] and cc-pVTZ basis set.[96] All the *ab initio* and DFT calculations were carried out using the GAUSSIAN 16[97] (B3LYP, ωB97XD, and evaluation of Franck−Condon factors) and MOLPRO 2021[98] (CCSD(T) and MP2) quantum chemistry program packages.

■ ASSOCIATED CONTENT

Data Availability Statement

The data that support the findings of this study are available in the article and the Supporting Information. Additional data are available from the corresponding authors upon reasonable request.

Supporting Information

The Supporting Information is available free of charge at https://pubs.acs.org/doi/10.1021/jacs.3c03816.

Precursor synthesis and characterization, additional mass spectra analysis, test reaction details, experimental conditions (Table S1), PIE curves (Figures S1−S4) and ms-TPE spectra (Figures S5 and S6) for other mass channels, PIE curves and ms-TPE spectra for the test reaction (Figures S7 and S8), and precursor NMR spectra (Figure S9−S13) (PDF)

■ AUTHOR INFORMATION

Corresponding Authors

Ralf I. Kaiser − *Department of Chemistry, University of Hawaii at Mānoa, Honolulu, Hawaii 96822, United States;* orcid.org/0000-0002-7233-7206; Email: ralfk@hawaii.edu

Alexander M. Mebel − *Department of Chemistry and Biochemistry, Florida International University, Miami, Florida 33199, United States;* orcid.org/0000-0002-7233-3133; Email: mebela@fiu.edu

Patrick Hemberger − *Paul Scherrer Institute, CH-5232 Villigen, PSI, Switzerland;* orcid.org/0000-0002-1251-4549; Email: patrick.hemberger@psi.ch

Authors

Shane J. Goettl − *Department of Chemistry, University of Hawaii at Mānoa, Honolulu, Hawaii 96822, United States*

Lotefa B. Tuli − *Department of Chemistry and Biochemistry, Florida International University, Miami, Florida 33199, United States*

Andrew M. Turner − *Department of Chemistry, University of Hawaii at Mānoa, Honolulu, Hawaii 96822, United States*

Yahaira Reyes − *Department of Chemistry and Biochemistry, Florida International University, Miami, Florida 33199, United States*

A. Hasan Howlader − *Department of Chemistry and Biochemistry, Florida International University, Miami, Florida 33199, United States;* Present Address: Department of Chemistry, Johns Hopkins University, Baltimore, Maryland 21218, United States

Stanislaw F. Wnuk − *Department of Chemistry and Biochemistry, Florida International University, Miami, Florida 33199, United States;* orcid.org/0000-0002-3111-3919

Complete contact information is available at: https://pubs.acs.org/10.1021/jacs.3c03816

Notes

The authors declare no competing financial interest.

■ ACKNOWLEDGMENTS

This work was supported by the U.S. Department of Energy, Basic Energy Sciences, by Grant No. DE-FG02-03ER15411 to the University of Hawaii at Manoa and No. DE-FG02-04ER15570 to Florida International University. We acknowledge the Instructional & Research Computing Center (IRCC, web: http://ircc.fiu.edu) at FIU and the National Energy Research Scientific Computing Center (NERSC) of the Office of Science in the U.S. Department of Energy for providing computing resources. The PEPICO measurements were performed at the VUV (x04db) beamline of the Swiss Light Source, located at the Paul Scherrer Institute, Villigen Switzerland.

■ REFERENCES

(1) Scholl, R.; Meyer, K. Synthese des anti-diperi-Dibenz-coronens und dessen Abbau zum Coronen (Hexabenzo-benzol). (Mitbearbeitet von Horst v. Hoeßle und Solon Brissimdji). *Ber. dtsch. Chem. Ges. A/B* **1932**, *65*, 902.

(2) Mercuri, F.; Baldoni, M.; Sgamellotti, A. Towards nano-organic chemistry: Perspectives for a bottom-up approach to the synthesis of low-dimensional carbon nanostructures. *Nanoscale* **2012**, *4*, 369.
(3) Liu, Z.; Chen, Z.; Wang, C.; Wang, H. I.; Wuttke, M.; Wang, X.-Y.; Bonn, M.; Chi, L.; Narita, A.; Müllen, K. Bottom-up, on-surface-synthesized armchair graphene nanoribbons for ultra-high-power micro-supercapacitors. *J. Am. Chem. Soc.* **2020**, *142*, 17881.
(4) Allen, M. J.; Tung, V. C.; Kaner, R. B. Honeycomb carbon: A review of graphene. *Chem. Rev.* **2010**, *110*, 132.
(5) Zhong, Q.; Hu, Y.; Niu, K.; Zhang, H.; Yang, B.; Ebeling, D.; Tschakert, J.; Cheng, T.; Schirmeisen, A.; Narita, A.; et al. Benzo-fused periacenes or double helicenes? Different cyclodehydrogenation pathways on surface and in solution. *J. Am. Chem. Soc.* **2019**, *141*, 7399.
(6) Pozo, I.; Guitián, E.; Pérez, D.; Peña, D. Synthesis of nanographenes, starphenes, and sterically congested polyarenes by aryne cyclotrimerization. *Acc. Chem. Res.* **2019**, *52*, 2472.
(7) Chen, Q.; Schollmeyer, D.; Müllen, K.; Narita, A. Synthesis of circumpyrene by alkyne benzannulation of brominated dibenzo[*hi,st*]-ovalene. *J. Am. Chem. Soc.* **2019**, *141*, 19994.
(8) Beyer, D.; Wang, S.; Pignedoli, C. A.; Melidonie, J.; Yuan, B.; Li, C.; Wilhelm, J.; Ruffieux, P.; Berger, R.; Müllen, K.; et al. Graphene nanoribbons derived from zigzag edge-encased poly(*para*-2,9-dibenzo[*bc,kl*]coronenylene) polymer chains. *J. Am. Chem. Soc.* **2019**, *141*, 2843.
(9) Fernández-García, J. M.; Evans, P. J.; Filippone, S.; Herranz, M. Á.; Martín, N. Chiral molecular carbon nanostructures. *Acc. Chem. Res.* **2019**, *52*, 1565.
(10) Metzger, R. M. Unimolecular electronics. *Chem. Rev.* **2015**, *115*, 5056.
(11) Han, W.; Kawakami, R. K.; Gmitra, M.; Fabian, J. Graphene spintronics. *Nat. Nanotechnol.* **2014**, *9*, 794.
(12) Loh, K. P.; Tong, S. W.; Wu, J. Graphene and graphene-like molecules: Prospects in solar cells. *J. Am. Chem. Soc.* **2016**, *138*, 1095.
(13) Mettry, M.; Hooley, R. J. In *Comprehensive Supramolecular Chemistry II*; Atwood, J. L., Ed.; Elsevier: Oxford, 2017, p 73.
(14) Xiao, J.; Yang, H.; Yin, Z.; Guo, J.; Boey, F.; Zhang, H.; Zhang, Q. Preparation, characterization, and photoswitching/light-emitting behaviors of coronene nanowires. *J. Mater. Chem.* **2011**, *21*, 1423.
(15) Reger, D.; Haines, P.; Amsharov, K. Y.; Schmidt, J. A.; Ullrich, T.; Bönisch, S.; Hampel, F.; Görling, A.; Nelson, J.; Jelfs, K. E.; et al. A family of superhelicenes: Easily tunable, chiral nanographenes by merging helicity with planar π systems. *Angew. Chem., Int. Ed.* **2021**, *60*, 18073.
(16) Xiao, X.; Cheng, Q.; Bao, S. T.; Jin, Z.; Sun, S.; Jiang, H.; Steigerwald, M. L.; Nuckolls, C. Single-handed helicene nanoribbons via transfer of chiral information. *J. Am. Chem. Soc.* **2022**, *144*, 20214.
(17) Zhao, X.; Sun, S.; Yang, F.; Li, Y. Atomic-scale evidence of catalyst evolution for the structure-controlled growth of single-walled carbon nanotubes. *Acc. Chem. Res.* **2022**, *55*, 3334.
(18) Scott, L. T.; Jackson, E. A.; Zhang, Q.; Steinberg, B. D.; Bancu, M.; Li, B. A short, rigid, structurally pure carbon nanotube by stepwise chemical synthesis. *J. Am. Chem. Soc.* **2012**, *134*, 107.
(19) Koenig, R. M.; Tian, H.-R.; Seeler, T. L.; Tepper, K. R.; Franklin, H. M.; Chen, Z.-C.; Xie, S.-Y.; Stevenson, S. Fullertubes: Cylindrical carbon with half-fullerene end-caps and tubular graphene belts, their chemical enrichment, crystallography of pristine C_{90}-$D_{5h}(1)$ and C_{100}-$D_{5d}(1)$ fullertubes, and isolation of C_{108}, C_{120}, C_{132}, and C_{156} cages of unknown structures. *J. Am. Chem. Soc.* **2020**, *142*, 15614.
(20) Schüßlbauer, C. M.; Krug, M.; Ullrich, T.; Franklin, H. M.; Stevenson, S.; Clark, T.; Guldi, D. M. Exploring the threshold between fullerenes and nanotubes: Characterizing isomerically pure, empty-caged, and tubular fullerenes D_{5h}-C_{90} and D_{5d}-C_{100}. *J. Am. Chem. Soc.* **2022**, *144*, 10825.
(21) Liu, X.; Bourret, E.; Noble, C. A.; Cover, K.; Koenig, R. M.; Huang, R.; Franklin, H. M.; Feng, X.; Bodnar, R. J.; Zhang, F.; et al. Gigantic C_{120} fullertubes: Prediction and experimental evidence for isomerically purified metallic [5,5] C_{120}-$D_{5d}(1)$ and nonmetallic [10,0] C_{120}-$D_{5h}(10766)$. *J. Am. Chem. Soc.* **2022**, *144*, 16287.
(22) Iijima, S. Helical microtubules of graphitic carbon. *Nature* **1991**, *354*, 56.
(23) Serrano, M. C.; Gutiérrez, M. C.; del Monte, F. Role of polymers in the design of 3D carbon nanotube-based scaffolds for biomedical applications. *Prog. Polym. Sci.* **2014**, *39*, 1448.
(24) Hirsch, A. The era of carbon allotropes. *Nat. Mater.* **2010**, *9*, 868.
(25) Draine, B. T. Interstellar dust grains. *Annu. Rev. Astron. Astrophys.* **2003**, *41*, 241.
(26) Martin, J. W.; Salamanca, M.; Kraft, M. Soot inception: Carbonaceous nanoparticle formation in flames. *Prog. Energy Combust. Sci.* **2022**, *88*, 100956.
(27) Duley, W. W. Polycyclic aromatic hydrocarbons, carbon nanoparticles and the diffuse interstellar bands. *Faraday Discuss.* **2006**, *133*, 415.
(28) Ricks, A. M.; Douberly, G. E.; Duncan, M. A. The infrared spectrum of protonated naphthalene and its relevance for the unidentified infrared bands. *Astrophys. J.* **2009**, *702*, 301.
(29) Becker, L.; Bunch, T. E. Fullerenes, fulleranes and polycyclic aromatic hydrocarbons in the Allende meteorite. *Meteorit. Planet. Sci.* **1997**, *32*, 479.
(30) de Vries, M. S.; Reihs, K.; Wendt, H. R.; Golden, W. G.; Hunziker, H. E.; Fleming, R.; Peterson, E.; Chang, S. A search for C_{60} in carbonaceous chondrites. *Geochim. Cosmochim. Acta* **1993**, *57*, 933.
(31) Plows, F. L.; Elsila, J. E.; Zare, R. N.; Buseck, P. R. Evidence that polycyclic aromatic hydrocarbons in two carbonaceous chondrites predate parent-body formation. *Geochim. Cosmochim. Acta* **2003**, *67*, 1429.
(32) Richter, H.; Grieco, W. J.; Howard, J. B. Formation mechanism of polycyclic aromatic hydrocarbons and fullerenes in premixed benzene flames. *Combust. Flame* **1999**, *119*, 1.
(33) Richter, H.; Howard, J. B. Formation and consumption of single-ring aromatic hydrocarbons and their precursors in premixed acetylene, ethylene and benzene flames. *Phys. Chem. Chem. Phys.* **2002**, *4*, 2038.
(34) Siegmann, K.; Hepp, H.; Sattler, K. Reactive dimerization: A new PAH growth mechanism in flames. *Combust. Sci. Technol.* **1995**, *109*, 165.
(35) Siegmann, K.; Sattler, K.; Siegmann, H. C. Clustering at high temperatures: carbon formation in combustion. *J. Electron Spectrosc. Relat. Phenom.* **2002**, *126*, 191.
(36) Mahamuni, G.; Rutherford, J.; Davis, J.; Molnar, E.; Posner, J. D.; Seto, E.; Korshin, G.; Novosselov, I. Excitatione-emission matrix spectroscopy for analysis of chemical composition of combustion generated particulate matter. *Environ. Sci. Technol.* **2020**, *54*, 8198.
(37) Wang, Y.; Raj, A.; Chung, S. H. Soot modeling of counterflow diffusion flames of ethylene-based binary mixture fuels. *Combust. Flame* **2015**, *162*, 586.
(38) Wang, Y.; Chung, S. H. Strain rate effect on sooting characteristics in laminar counterflow diffusion flames. *Combust. Flame* **2016**, *165*, 433.
(39) Liu, A.; Garcia, C. E.; Sewerin, F.; Williams, B. A. O.; Rigopoulos, S. Population balance modelling and laser diagnostic validation of soot particle evolution in laminar ethylene diffusion flames. *Combust. Flame* **2020**, *221*, 384.
(40) Zhang, Y.; Xiao, B.; Li, Y.; Liu, P.; Zhan, R.; Huang, Z.; Lin, H. LIF diagnostics for selective and quantitative measurement of PAHs in laminar premixed flames. *Combust. Flame* **2020**, *222*, 5.
(41) Park, S.; Wang, Y.; Chung, S. H.; Sarathy, S. M. Compositional effects on PAH and soot formation in counterflow diffusion flames of gasoline surrogate fuels. *Combust. Flame* **2017**, *178*, 46.
(42) Faccinetto, A.; Focsa, C.; Desgroux, P.; Ziskind, M. Progress toward the quantitative analysis of PAHs adsorbed on soot by laser desorption/laser ionization/time-of-flight mass spectrometry. *Environ. Sci. Technol.* **2015**, *49*, 10510.

https://doi.org/10.1021/jacs.3c03816
J. Am. Chem. Soc. 2023, 145, 15443−15455

(43) Totton, T. S.; Misquitta, A. J.; Kraft, M. A quantitative study of the clustering of polycyclic aromatic hydrocarbons at high temperatures. *Phys. Chem. Chem. Phys.* **2012**, *14*, 4081.
(44) Mao, Q.; Zhou, J.; Luo, K. H.; van Duin, A. C. T. Atomistic insights into the dynamics of binary collisions between gaseous molecules and polycyclic aromatic hydrocarbon dimers. *Phys. Chem. Chem. Phys.* **2019**, *21*, 3849.
(45) Hernández-Rojas, J.; Calvo, F. Coarse-grained modeling of the nucleation of polycyclic aromatic hydrocarbons into soot precursors. *Phys. Chem. Chem. Phys.* **2019**, *21*, 5123.
(46) Mao, Q.; Hou, D.; Luo, K. H.; You, X. Dimerization of polycyclic aromatic hydrocarbon molecules and radicals under flame conditions. *J. Phys. Chem. A* **2018**, *122*, 8701.
(47) Jiang, X.; Zhou, K.; Xiao, M.; Sun, K.; Wang, Y. Stochastic simulation of soot formation evolution in counterflow diffusion flames. *J. Nanotechnol.* **2018**, *2018*, 9479582.
(48) Mao, Q.; Ren, Y.; Luo, K. H.; Duin, A. C. T. v. Dynamics and kinetics of reversible homo-molecular dimerization of polycyclic aromatic hydrocarbons. *J. Chem. Phys.* **2017**, *147*, 244305.
(49) Kohse-Höinghaus, K. A new era for combustion research. *Pure Appl. Chem.* **2019**, *91*, 271.
(50) Cherchneff, I. The inner wind of IRC+10216 revisited: New exotic chemistry and diagnostic for dust condensation in carbon stars. *Astron. Astrophys.* **2012**, *545*, A12.
(51) Liu, P.; He, Z.; Hou, G.-L.; Guan, B.; Lin, H.; Huang, Z. The diagnostics of laser-induced fluorescence (LIF) spectra of PAHs in flame with TD-DFT: Special focus on five-membered ring. *J. Phys. Chem. A* **2015**, *119*, 13009.
(52) Wang, Y.; Raj, A.; Chung, S. H. A PAH growth mechanism and synergistic effect on PAH formation in counterflow diffusion flames. *Combust. Flame* **2013**, *160*, 1667.
(53) Mohammed, S.; Raj, A.; Al Shoaibi, A.; Sivashanmugam, P. Formation of polycyclic aromatic hydrocarbons in Claus process from contaminants in H_2S feed gas. *Chem. Eng. Sci.* **2015**, *137*, 91.
(54) Keita, M.; Nicolle, A.; Bakali, A. E. A wide range kinetic modeling study of PAH formation from liquid transportation fuels combustion. *Combust. Flame* **2016**, *174*, 50.
(55) Norinaga, K.; Deutschmann, O. Detailed kinetic modeling of gas-phase reactions in the chemical vapor deposition of carbon from light hydrocarbons. *Ind. Eng. Chem. Res.* **2007**, *46*, 3547.
(56) Norinaga, K.; Deutschmann, O.; Saegusa, N.; Hayashi, J.-i. Analysis of pyrolysis products from light hydrocarbons and kinetic modeling for growth of polycyclic aromatic hydrocarbons with detailed chemistry. *J. Anal. Appl. Pyrolysis* **2009**, *86*, 148.
(57) Kousoku, A.; Norinaga, K.; Miura, K. Extended detailed chemical kinetic model for benzene pyrolysis with new reaction pathways including oligomer formation. *Ind. Eng. Chem. Res.* **2014**, *53*, 7956.
(58) Matsugi, A.; Miyoshi, A. Modeling of two- and three-ring aromatics formation in the pyrolysis of toluene. *Proc. Combust. Inst.* **2013**, *34*, 269.
(59) Raj, A.; Prada, I. D. C.; Amer, A. A.; Chung, S. H. A reaction mechanism for gasoline surrogate fuels for large polycyclic aromatic hydrocarbons. *Combust. Flame* **2012**, *159*, 500.
(60) Selvaraj, P.; Arias, P. G.; Lee, B. J.; Im, H. G.; Wang, Y.; Gao, Y.; Park, S.; Sarathy, S. M.; Lu, T.; Chung, S. H. A computational study of ethylene-air sooting flames: Effects of large polycyclic aromatic hydrocarbons. *Combust. Flame* **2016**, *163*, 427.
(61) Zhou, D.; Yang, S. Soot-based global pathway analysis: Soot formation and evolution at elevated pressures in co-flow diffusion flames. *Combust. Flame* **2021**, *227*, 255.
(62) Li, M.; Xu, G.; Zhao, Y.; Li, G.; Wang, Z. Influence of n-butanol addition on C_3H_3 formation in n-butane combustion. *Kinet. Catal.* **2019**, *60*, 8.
(63) Dong, X.; Chang, Y.; Niu, B.; Jia, M. Development of a practical reaction model of polycyclic aromatic hydrocarbon (PAH) formation and oxidation for diesel surrogate fuel. *Fuel* **2020**, *267*, 117159.
(64) Li, Y.; Lou, B.; Tang, W.; Abubakar, S.; Liu, G. A more realistic skeletal mechanism with compact size for n-butanol combustion in diesel engines. *Proc. Inst. Mech. Eng., Part D* **2021**, *235*, 3082.
(65) Wang, Y.; Han, W.; Attili, A.; Chen, Z. Numerical analysis of very rich propagating spherical flames: Soot formation and its impact on the determination of laminar flame speed. *Combust. Flame* **2022**, *237*, 111860.
(66) Tuli, L. B.; Goettl, S. J.; Turner, A. M.; Howlader, A. H.; Hemberger, P.; Wnuk, S. F.; Guo, T.; Mebel, A. M.; Kaiser, R. I. Gas phase synthesis of the C40 nano bowl $C_{40}H_{10}$. *Nat. Commun.* **2023**, *14*, 1527.
(67) Mercier, X.; Faccinetto, A.; Batut, S.; Vanhove, G.; Božanić, D.; Hróćmarsson, H.; Garcia, G. A.; Nahon, L. Selective identification of cyclopentaring-fused PAHs and side-substituted PAHs in a low pressure premixed sooting flame by photoelectron photoion coincidence spectroscopy. *Phys. Chem. Chem. Phys.* **2020**, *22*, 15926.
(68) Bréchignac, P.; Garcia, G. A.; Falvo, C.; Joblin, C.; Kokkin, D.; Bonnamy, A.; Parneix, P.; Pino, T.; Pirali, O.; Mulas, G.; et al. Photoionization of cold gas phase coronene and its clusters: Autoionization resonances in monomer, dimer, and trimer and electronic structure of monomer cation. *J. Chem. Phys.* **2014**, *141*, 164325.
(69) Bourgalais, J.; Herbinet, O.; Carstensen, H.-H.; Debleza, J.; Garcia, G. A.; Arnoux, P.; Tran, L. S.; Vanhove, G.; Liu, B.; Wang, Z.; et al. Jet-stirred reactor study of low-temperature neopentane oxidation: A combined theoretical, chromatographic, mass spectrometric, and PEPICO analysis. *Energy Fuels* **2021**, *35*, 19689.
(70) Hemberger, P.; Bodi, A.; Bierkandt, T.; Köhler, M.; Kaczmarek, D.; Kasper, T. Photoelectron photoion coincidence spectroscopy provides mechanistic insights in fuel synthesis and conversion. *Energy Fuels* **2021**, *35*, 16265.
(71) Hemberger, P.; Bodi, A.; Schon, C.; Steinbauer, M.; Fischer, K. H.; Kaiser, C.; Fischer, I. A pass too far: dissociation of internal energy selected paracyclophane cations, theory and experiment. *Phys. Chem. Chem. Phys.* **2012**, *14*, 11920.
(72) Pan, Z.; Puente-Urbina, A.; Bodi, A.; van Bokhoven, J. A.; Hemberger, P. Isomer-dependent catalytic pyrolysis mechanism of the lignin model compounds catechol, resorcinol and hydroquinone. *Chem. Sci.* **2021**, *12*, 3161.
(73) Rösch, D.; Caravan, R. L.; Taatjes, C. A.; Au, K.; Almeida, R.; Osborn, D. L. Absolute photoionization cross section of the simplest enol, vinyl alcohol. *J. Phys. Chem. A* **2021**, *125*, 7920.
(74) Bodi, A.; Hemberger, P.; Osborn, D. L.; Sztáray, B. Mass-resolved isomer-selective chemical analysis with imaging photoelectron photoion coincidence spectroscopy. *J. Phys. Chem. Lett.* **2013**, *4*, 2948.
(75) Johansson, K. O.; Campbell, M. F.; Elvati, P.; Schrader, P. E.; Zádor, J.; Richards-Henderson, N. K.; Wilson, K. R.; Violi, A.; Michelsen, H. A. Photoionization efficiencies of five polycyclic aromatic hydrocarbons. *J. Phys. Chem. A* **2017**, *121*, 4447.
(76) Hirata, S.; Head-Gordon, M.; Szczepanski, J.; Vala, M. Time-dependent density functional study of the electronic excited states of polycyclic aromatic hydrocarbon radical ions. *J. Phys. Chem. A* **2003**, *107*, 4940.
(77) Hemberger, P.; Wu, X.; Pan, Z.; Bodi, A. Continuous pyrolysis microreactors: Hot sources with little cooling? New insights utilizing cation velocity map imaging and threshold photoelectron spectroscopy. *J. Phys. Chem. A* **2022**, *126*, 2196.
(78) Zhao, L.; Prendergast, M. B.; Kaiser, R. I.; Xu, B.; Ablikim, U.; Ahmed, M.; Sun, B. J.; Chen, Y. L.; Chang, A. H. H.; Mohamed, R. K. Synthesis of polycyclic aromatic hydrocarbons by phenyl addition-dehydrocyclization: The third way. *Angew. Chem.* **2019**, *131*, 17603.
(79) Bodi, A.; Johnson, M.; Gerber, T.; Gengeliczki, Z.; Sztáray, B.; Baer, T. Imaging photoelectron photoion coincidence spectroscopy with velocity focusing electron optics. *Rev. Sci. Instrum.* **2009**, *80*, 034101.
(80) Johnson, M.; Bodi, A.; Schulz, L.; Gerber, T. Vacuum ultraviolet beamline at the Swiss Light Source for chemical dynamics

studies. *Nucl. Instrum. Methods Phys. Res. A: Accel. Spectrom. Detect. Assoc. Equip.* **2009**, *610*, 597.
(81) Bouwman, J.; Bodi, A.; Hemberger, P. Nitrogen matters: the difference between PANH and PAH formation. *Phys. Chem. Chem. Phys.* **2018**, *20*, 29910.
(82) Hemberger, P.; van Bokhoven, J. A.; Pérez-Ramírez, J.; Bodi, A. New analytical tools for advanced mechanistic studies in catalysis: photoionization and photoelectron photoion coincidence spectroscopy. *Catal. Sci. Technol.* **2020**, *10*, 1975.
(83) Mendez-Vega, E.; Sander, W.; Hemberger, P. Isomer-selective threshold photoelectron spectra of phenylnitrene and its thermal rearrangement products. *J. Phys. Chem. A* **2020**, *124*, 3836.
(84) Grimm, S.; Baik, S.-J.; Hemberger, P.; Bodi, A.; Kempf, A. M.; Kasper, T.; Atakan, B. Gas-phase aluminium acetylacetonate decomposition: revision of the current mechanism by VUV synchrotron radiation. *Phys. Chem. Chem. Phys.* **2021**, *23*, 15059.
(85) Sztáray, B.; Baer, T. Suppression of hot electrons in threshold photoelectron photoion coincidence spectroscopy using velocity focusing optics. *Rev. Sci. Instrum.* **2003**, *74*, 3763.
(86) Chupka, W. A. Factors affecting lifetimes and resolution of Rydberg states observed in zero-electron-kinetic-energy spectroscopy. *J. Chem. Phys.* **1993**, *98*, 4520.
(87) Becke, A. D. Density-functional thermochemistry. III. The role of exact exchange. *J. Chem. Phys.* **1993**, *98*, 5648.
(88) Lee, C.; Yang, W.; Parr, R. G. Development of the Colle-Salvetti correlation-energy formula into a functional of the electron density. *Phys. Rev. B* **1988**, *37*, 785.
(89) Curtiss, L. A.; Raghavachari, K.; Redfern, P. C.; Rassolov, V.; Pople, J. A. Gaussian-3 (G3) theory for molecules containing first and second-row atoms. *J. Chem. Phys.* **1998**, *109*, 7764.
(90) Curtiss, L. A.; Raghavachari, K.; Redfern, P. C.; Baboul, A. G.; Pople, J. A. Gaussian-3 theory using coupled cluster energies. *Chem. Phys. Lett.* **1999**, *314*, 101.
(91) Baboul, A. G.; Curtiss, L. A.; Redfern, P. C.; Raghavachari, K. Gaussian-3 theory using density functional geometries and zero-point energies. *J. Chem. Phys.* **1999**, *110*, 7650.
(92) Barone, V.; Bloino, J.; Biczysko, M.; Santoro, F. Fully integrated approach to compute vibrationally resolved optical spectra: From small molecules to macrosystems. *J. Chem. Theory Comput.* **2009**, *5*, 540.
(93) Furche, F.; Ahlrichs, R. Adiabatic time-dependent density functional methods for excited state properties. *J. Chem. Phys.* **2002**, *117*, 7433.
(94) Scalmani, G.; Frisch, M. J.; Mennucci, B.; Tomasi, J.; Cammi, R.; Barone, V. Geometries and properties of excited states in the gas phase and in solution: Theory and application of a time-dependent density functional theory polarizable continuum model. *J. Chem. Phys.* **2006**, *124*, 094107.
(95) Chai, J.-D.; Head-Gordon, M. Long-range corrected hybrid density functionals with damped atom-atom dispersion corrections. *Phys. Chem. Chem. Phys.* **2008**, *10*, 6615.
(96) Dunning, T. H., Jr Gaussian basis sets for use in correlated molecular calculations. I. The atoms boron through neon and hydrogen. *J. Chem. Phys.* **1989**, *90*, 1007.
(97) Frisch, M. J.; Trucks, G. W.; Schlegel, H. B.; Scuseria, G. E.; Robb, M. A.; Cheeseman, J. R.; Scalmani, G.; Barone, V.; Petersson, G. A.; Nakatsuji, H.; et al. *GAUSSIAN 16, Revision C.1*; Gaussian, Inc.: Wallingford, CT, 2019; see http://www.gaussian.com (2022−03−21).
(98) Werner, H.-J.; Knowles, P. J.; Knizia, G.; Manby, F. R.; Schütz, M.; Celani, P.; Györffy, W.; Kats, D.; Korona, T.; Lindh, R.; et al. *MOLPRO, version 2021.2, a package of ab initio programs*; University of Cardiff: Cardiff, UK, 2021; see http://www.molpro.net (2022−03−21).

https://doi.org/10.1021/jacs.3c03816
J. Am. Chem. Soc. 2023, 145, 15443−15455